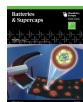VIP *Very Important Paper*

Computational Model for Predicting Particle Fracture During Electrode Calendering

Jiahui Xu,[a, b] Brayan Paredes-Goyes,[a, b] Zeliang Su,[a, b] Mario Scheel,[d] Timm Weitkamp,[d] Arnaud Demortière,[a, b, c] and Alejandro A. Franco*[a, b, c, e]

In the context of calling for low carbon emissions, lithium-ion batteries (LIBs) have been widely concerned as a power source for electric vehicles, so the fundamental science behind their manufacturing has attracted much attention in recent years. Calendering is an important step of the LIB electrode manufacturing process, and associated changes in the electrode microstructure and mechanical properties are worthy of study. In this work, we report the observed cracking of active material (AM) particles due to calendering pressure under *ex situ* X-ray nano tomography experiments. We developed an innovative 3D discrete element method (DEM) model with bonded connections to physically mimic the calendering process using real AM particle shapes derived from the tomography experiments. The DEM model can well predict the change of the morphology of the dry electrode under pressure, and the changes of the applied pressure and porosity are consistent with the experimental values. At the same time, the model is able to simulate the secondary AM particles cracking by the fracture of the bonds under force. Our model is the first of its kind that can predict the fracture of the secondary particles along the calendering process. This work provides a tool for guidance in the manufacturing of optimized LIB electrodes.

Introduction

Three decades after the first commercial rechargeable lithium-ion battery (LIB) was introduced, LIBs have become an omnipresent technology in our lives. In the past fifteen years, electric transportation has grown in popularity in response to environmental constraints.[1] However, for private transportation, improving the battery energy and power densities while reducing costs is still a problem worthy of research.[2] There is

[a] J. Xu, Dr. B. Paredes-Goyes, Dr. Z. Su, Dr. A. Demortière,
Prof. Dr. A. A. Franco
Laboratoire de Réactivité et Chimie des Solides (LRCS)
UMR CNRS 7314
Université de Picardie Jules Verne
Hub de l'Energie
15 rue Baudelocque, 80039 Amiens Cedex (France)
E-mail: alejandro.franco@u-picardie.fr

[b] J. Xu, Dr. B. Paredes-Goyes, Dr. Z. Su, Dr. A. Demortière, Prof. Dr. A. A. Franco
Réseau sur le Stockage Electrochimique de l'Energie (RS2E)
FR CNRS 3459, Hub de l'Energie
15 rue Baudelocque, 80039 Amiens Cedex (France)

[c] Dr. A. Demortière, Prof. Dr. A. A. Franco
ALISTORE-European Research Institute
FR CNRS 3104, Hub de l'Energie
15 rue Baudelocque, 80039 Amiens Cedex (France)

[d] Dr. M. Scheel, Dr. T. Weitkamp
Synchrotron SOLEIL
91190 Saint-Aubin (France)

[e] Prof. Dr. A. A. Franco
Institut Universitaire de France
103 Boulevard Saint Michel, 75005 Paris (France)

no doubt that material research plays a vital role in finding solutions to this problem, as the energy and power densities, the cycle life, and the safety of LIBs are closely related to the performance of the materials. Meanwhile, the manufacturing process is crucial as it impacts the battery quality and cost. The electrode is the most important part in a battery cell since the electrochemical reactions take place there. Its manufacturing process is usually as follows: dry and wet mixing to prepare a slurry, followed by its coating, drying, calendering, dimension control, and final drying.[3] During the calendering step, as the electrode thickness decreases under compression, the porosity decreases and the electronic conductivity increases, resulting in improved electrode volumetric energy density.[4] Davoodabadi *et al.* verified that the wetting properties of the electrode can be affected by the calendering process.[5] For graphite anode, the wettability is improved through light calendering, followed by a decrease in wettability as the degree of calendering increases.[6] There is no doubt that the parameters of calendering affect the electrode properties. It is reported that pressures, temperatures, and the speed of calendering have an impact on electrode performance,[7,8] which also depends on the active material (AM) particle size distribution.[9–11] The X-ray Computed Tomography (XCT) has confirmed that the irreversible effects of calendering on electrode morphological change have a significant influence on electrochemical performance.[11,12] Likewise, the deformation and rotation of the AM were observed. Sim *et al.*[13] reported the cracking and fusion in high-nickel cathode materials during calendering by using scanning electron microscopy, which alleviated electrochemical capacity decay. AM particle cracking can lead to a deterioration of electrode connectivity and thereby impact electrochemical performance,[14] however most of studies so far have focused on the cracking of AM during electrochemical charge and discharge. Huttner *et al.* proposed in their study that the cracks

Batteries & Supercaps | Research Article
doi.org/10.1002/batt.202300371

Chemistry
Europe
European Chemical
Societies Publishing

and breakage of NMC622 during the calendering process lead to a larger surface area of the cathode, which is able to absorb higher moisture after compression. On the one hand, cracking can improve the penetration of electrolytes in the AM particles, thereby improving lithium ion transport. On the other hand, increased moisture may affect the connection between the electrode and the current collector.[15] As a consequence, it is important to study the calendering process' effect on the cracks of the AM particles.

The XCT technique, a state-of-the-art non-destructive method, is increasingly used in battery research. It gives researchers access to the three-dimensional (3D) microstructure of battery electrodes, providing valuable insights into their intricate architectures, secondary particle morphologies, and the layout of conductive percolated networks.[16–18] The microstructure datasets can be used to investigate and quantitatively study electrode properties such as porosity, tortuosity factor, specific reaction area, anisotropy, and homogeneity. Such technique has been used for LIBs on materials like graphite,[12,16,17] $LiNi_xMn_yCo_{1-x-y}O_2$ (NMC),[12,19,20] $LiFePO_4$[21] and $LiCoO_2$[12,20] both for lab-prepared and commercial LIBs. It also enables the tracking of the electrode size, shape, and network morphology changes like AM cracking and irreversible deformation due to mechanical factors during and after the manufacturing process.[11] Additionally, a variety of algorithms based on machine learning have been developed to support the segmentation of each material phase (AM, carbon-binder, and pores) in the grayscale image dataset.[22,23]

Computational models are popular in this digital age and offer a plethora of interesting capabilities to gain insights into the electrode microstructure. To link with industrial production, digital models for different steps of the LIB manufacturing process have been developed.[24–26] Several studies have applied computational simulation to investigate the LIB electrode architecture changes during the manufacturing process. Sangros Gimenez et al.[27] simulated the electrode behavior in the calendering process by a discrete element method (DEM) approach by describing explicitly only the active material particles. Srivastava et al.[28] predicted the electrode properties by controlling binder adhesion during the manufacturing process by using a combination of discrete element and colloidal dynamics methods. Nikpour et al.[29,30] developed the multi-phase smoothed particle model to study the electrode heterogeneity and the electrode properties. Ge et al.[31,32] performed calendering DEM calculations using X-ray tomography data of electrodes as initial microstructures for the simulations, and implicitly representing the binder effect by employing a bond model between AM particles. Lippke et al.[33] used DEM to identify the impact of the electrode preheating on the calendering process. Wang et al.[34] used a DEM with an additional bond model to describe the microstructure evolution under stress and discover the mechanical integrity of the active layer is influenced by the binder content and the active particle size distribution. Asylbekov et al.[35] used a microscale Continuum Fluid Dynamics (CFD)-DEM to investigate the breaking behavior of carbon black aggregates due to the shear stress during the mixing process. Lundkvist et al.[36] developed a method to simulate the electrode creation and calendering with DEM, which is able to capture the unloaded stiffness behavior induced by the viscoelastic binder. All these works (except references [28,29]) do not account for an explicit representation of the carbon-binder domain phase. In our ARTISTIC project,[37] funded by European Research Council, we developed a series of pioneering sequentially coupled 3D-resolved physical-based models to represent the different steps of the LIB electrode manufacturing process by using coarse-grained molecular dynamics and DEM. This digital twin of the electrode manufacturing process, allows to predict, as a function of the manufacturing process parameters, the spatial location of both active and inactive phases in a 3D-resolved fashion.[38–43]

Earlier, we reported the introduction of real particle shapes, obtained by XCT, into our ARTISTIC manufacturing process model based on coarse-grained molecular dynamics (CGMD) and DEM.[44] In this model, the secondary AM particles, consisting of spherical primary particles, represent the AM in the electrode manufacturing processes. Spherical particles are used to mimic the carbon binder domain (CBD) consisting of carbon, binder, and nanopores. In this work, we performed an *ex situ* nanoscale XCT experiment on the electrode before and after the calendering process and assessed the fracture inside the secondary particles. Therefore, we used and optimized the existing model to further investigate the mechanical behavior of the electrode and probe the effect of calendering pressure on the particle cracking.

Experimental Analysis

Sample preparation

$LiNi_{0.33}Co_{0.33}Mn_{0.33}O_2$ (NMC111) (Umicore), carbon black (C-NERGY™ super C65) and Polyvinylidene fluoride (PVdF) (Solef™ 5130/1001, Solvay) are premixed in a weight ratio of 96:2:2 overnight. N-Methyl-2-pyrrolidone (NMP) is then added until the desired solid content is reached. The mixture is performed in a Dispermat CV3-PLUS high-shear mixer for 2 h at 25 °C. Then, the slurry is coated over a 22.5 μm thick Aluminum current collector by using a comma-coater prototype-grade machine (PDL250, People & Technology, Korea) and passes through two ovens with temperatures of 85 °C and 95 °C. After drying, the electrodes are calendered in a prototype-grade lap press calender (BPN250, People & Technology, Korea) under various roll gaps and at a constant line speed of 0.54 m/min at 60 °C. The calendering pressures were obtained from a calculation by using the roll gaps and the thickness of the electrode, which was calibrated by measuring the applied force of the corresponding roll gap through the utilization of a force sensor film (ELF measuring system equipped with FlexiForce sensors, Tekscan).[7]

Small electrode pieces were cut from the center of the electrode and glued horizontally by epoxy onto the metal needles. The tops of the electrodes were cut by a laser-equipped microdissector into the size that corresponds to the field of view used in the XCT experiment.

X-ray nano computed tomography

The X-ray nano tomographic analysis of the calendered electrode under different compression pressures was performed at the beamline Anatomix of Synchrotron SOLEIL, France[45] where transmission X-ray microscopy (TXM) instrument was used in absorption mode.[46] The scans were conducted with a monochromatic X-ray beam of photon energy 8.327 keV using a TXM configuration. The data sets are collected in different ways. 500 projections were acquired over 180° with an exposure time of 500 ms per two-dimensional (2D) image or 1000 projections were acquired over 360° with an exposure time of 500 ms with using an offset of 15 μm. Volumes were reconstructed with PyHST2[47] (ESRF, Grenoble, France). A smoothing filter was applied to denoise the images. The pixel size of the TXM and voxel size in the reconstructed volumes was 41 nm. The regions of interest were cropped out to be further studied.

To reduce or eliminate the noise and blurriness caused by image artifacts, the images were preprocessed prior to analysis. A non-local means filter was applied, followed by an unsharp mask to enhance the edges of all tomographic data. Then the machine learning segmentation plugin Trainable Weka,[48] based on the random Forest algorithm in the FIJI software suite, a distribution of the ImageJ software, was used to segment the 3D data into different phases. The methodology involved extracting features from images using various filters and a random forest algorithm for classification.

Results and Discussion

The electrode of a thickness of 114 μm was calendered between roll gaps of 21 μm and 6 μm. The respective pressures, the mass and thickness measured, and the porosity calculated are shown in Table 1. It is worth pointing out that these gaps refer to the gap between two rolls before calendering. An *in-house* experiment was previously conducted to establish a formula that relates the pre-calendering gap and the thickness of the uncalendered electrode to the applied pressure. Therefore, we can calculate the calendering pressure. During the calendering and post-calendering phases, this gap usually increases due to the forces exerted by the electrode on the roll.

The 2D slice images of these electrodes obtained from the nano-XCT are shown in Figure 1 (uncalendered and calendered under 150 MPa) and Figure S1 (calendered under 80 MPa). It can be clearly seen that the AM particles before calendering have already pores caused by material synthesis, but the particle structure is intact without cracks. As the pressure on the electrodes increased, the particles remained relatively intact at 80 MPa. At a pressure of 150 MPa, the particles showed obvious cracks.

The 3D images with gray values of the electrode before calendering and calendered under 150 MPa were segmented into 3 phases: AM, macro pores, and the nano-cracks. The triphasic image stacks were imported into the commercial software package Avizo V9.4 (Thermo Fisher Scientific)[49] for visualization. The 3D visualization is presented in Figure 1 and the voxel size in the 3D particle volumes is $41\times41\times41$ nm^3. Among the 3D volumes, only the AM phase and nano-cracks are visualized, and the macro pore phase is presented as the void in the volumes. The calendering process evidently influences the electrode density, as shown in Figure 1. Several individual particles were selected to demonstrate the intrinsic pores inside the AM particles and the nano-cracking due to the high pressure during the calendering process. The 3D visualization clearly shows the presence of cracks within the secondary particles after compression. The cracks are not evenly distributed or exist in every secondary particle. However, due to
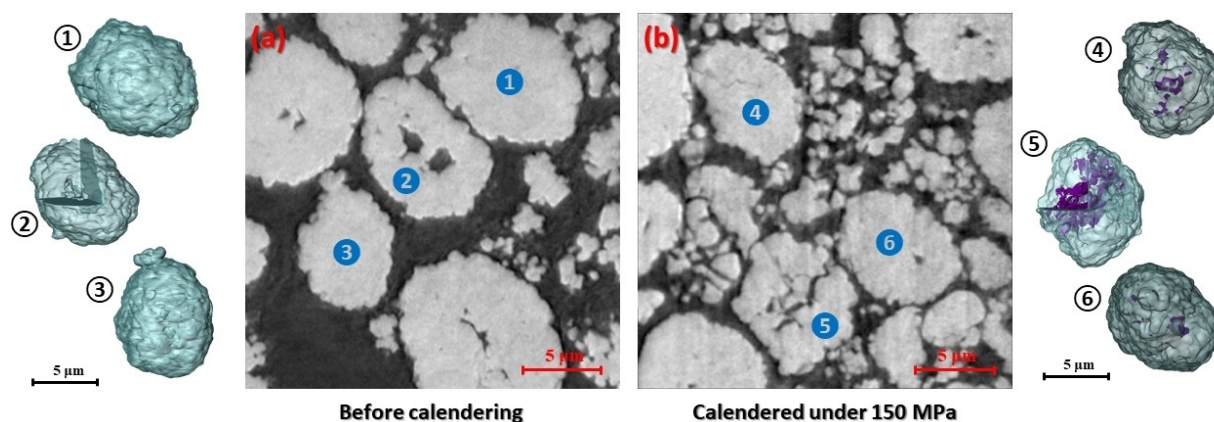
Table 1. The experimental information of the electrodes.

Roll gap [μm]	Corresponding pressure [MPa]	Mass [mg]	Thickness [μm]	Porosity [%]
–	0	22.37 ± 0.29	99.03 ± 0.87	47.97 ± 0.87
21	80	22.97 ± 0.11	79.67 ± 0.06	27.75 ± 0.23
6	150	22.30 ± 0.68	75.4 ± 0.79	25.17 ± 1.2

Before calendering

Calendered under 150 MPa

Figure 1. Nano XCT. Virtual slices and 3D renderings of the electrode, a) before calendering; b) calendered under 150 MPa. The individual particles are selected and presented in 3D. In the 3D renderings, the surfaces of the particles and the nano cracking are indicated in turquoise and violet, respectively. Particles 2 and 5 are sectioned to reveal internal structures. Scale bars: 5 μm.

Batteries & Supercaps

Research Article
doi.org/10.1002/batt.202300371

Chemistry Europe
European Chemical
Societies Publishing

the small size of our electrode volume, the cracks could not be accurately quantified. Another micro-scale *ex situ* XCT experiment was made to study the change of porosity and tortuosity factor of the electrode after calendering, the results are shown in Figure S2 in Supporting Information. Due to experimental limitations, it is difficult to obtain *in operando* the mechanical behavior of particles under each pressure. We therefore developed a new physical model to predict the fracture of secondary particles during the calendering process.

Numerical Analysis

Methods

The calendering process is modeled at the particle scale using DEM.[50] In addition to AM, we explicitly consider the CBD, which allows the obtention of more reliable mesostructures.[41] The CBD domain is represented by spherical particles with a diameter of 1.16 μm with a nanoporosity of 27%. The secondary AM particles present the realistic shape obtained by X-ray microcomputed tomography and particle size distribution (PSD) from the experimental statistics, as reported in our previous work.[39][44] These secondary particles are composed of spherical AM primary particles. The calender rolls and current collector are represented by a top and a bottom plane respectively, more information can be found in our earlier work.[41] The simulation box has a periodic boundary condition in the direction parallel to the plane and the current collector.

The new position of each particle is determined by the contact and external body forces, in our case the latter consisting only of gravity. Every pair of particles in contact experiences an elastic Hertzian force composed of normal and tangential components:

$$F_E^n = k_n \delta \, \mathbf{n} - \gamma_n \mathbf{v}_r^n \tag{1}$$

$$F_E^t = -min\left(\mu_t \left| F_E^n \right|, \left| -k_t \mathbf{S}_t - \gamma_t \mathbf{v}_r^t \right|\right) \, \mathbf{t} \tag{2}$$

where k_n, k_t are the normal and tangential elastic constants, while γ_n, γ_t are the normal and tangential viscoelastic damping constants. These constants are estimated from the following particle properties: Young's modulus E_p, Poisson's ratio Po_p and restitution coefficient e_p. In the equations, δ is the overlap distance, $\mathbf{v}_r^n$, $\mathbf{v}_r^t$ are the normal and tangential relative velocities and $\mathbf{S}_t$ is the accumulated tangential displacement. $\mathbf{n}$, $\mathbf{t}$ are the normal and tangential unit vectors.

The secondary AM particles and the CBD particles are also subjected to cohesion forces, here represented by a Simplified Johnson-Kendall-Roberts model (SJKR). This force is an attractive normal force given by:

$$F_C = -c_{CED} \, A_{COH} \, \mathbf{n} \tag{3}$$

where c_{CED} is the cohesion energy density and A_{COH} is the contact area (sphere-sphere). On the other hand, the existing sintering force between primary particles belonging to the

same secondary particle is represented by the bonded-particle model (BPM).[51] The normal and tangential incremental forces of a bond are calculated at each timestep following:[52]

$$\Delta F_B^n = \frac{E_b A_b}{l_b} \mathbf{v}_r^n \Delta t \tag{4}$$

$$\Delta F_B^t = \frac{(E_b/2(1 + Po_b)) A_b}{l_b} \mathbf{v}_r^t \Delta t \tag{5}$$

where A_b, l_b are the cross-section area and the length of the assumed cylindrical bond. E_b, Po_b are the Young's modulus and the Poisson's ratio of the bond. In order to decrease the free parameters, these two bond properties are set to the same value as the particle parameters. The latter (E_p, Po_p) are straightforwardly calibrated by fitting the maximum pressure during calendering.

Similar expressions can be found in Ref. [52] to calculate the axial ΔM_B^n and shear ΔM_B^t incremental moments of the bonds. In this way, the beam theory allows to calculate the maximum normal and shear stresses at the bond following:[51]

$$\sigma_B^n = \frac{-\left| F_B^n \right|}{A_b} + \frac{\left| M_B^t \right| R_{min}}{I} \tag{6}$$

$$\sigma_B^t = \frac{\left| F_B^t \right|}{A_b} + \frac{\left| M_B^n \right| R_{min}}{J} \tag{7}$$

where R_{min} is the lower of the radii of particles i and j, while I, J are the moment of inertia and the polar moment of inertia of the cross section of the bond.

Following the failure criteria proposed by the BPM, a bond breaks if the maximum normal stress is higher than the bond's normal strength ($\sigma_B^n \geq \sigma_B^{cn}$) or if the maximum tangential stress is higher than the bond shear strength ($\sigma_B^t \geq \sigma_B^{ct}$). Other failure criteria can be found in Ref. [53]. For normal and shear breakage to be possible, $\sigma_B^{cn} = \sigma_B^{ct}$.[51] This strength value at the bond level should be found by calibration. Here, as a first DEM model for the fracture of NMC particles, a simple parametric study is performed to elucidate the influence of this value, as shown in the Figure S3. The parameters used for the model are presented in the Supporting Information in detail.

The interaction among primary particles of the same secondary particle should be completely described by its corresponding bonds. However, the addition of cohesion (SJKR) between primary particles in our simulations was required to ensure the stability of the secondary particle. This limitation will be further investigated in future work.

The initial electrode microstructure for calendering was derived from the simulation result of drying in our previous work[44] to maintain continuity in our manufacturing simulations. The real shapes of the secondary particles in the simulation were extracted from the micro-scale XCT, which is reported in detail in that same publication, obtained at the P05 beamline of the PETRA III synchrotron light source at a pixel size of 0.64 μm. The methods used for the image digitization and the initial structure generation are described in detail in

Batteries & Supercaps

Research Article
doi.org/10.1002/batt.202300371

Chemistry
Europe

European Chemical
Societies Publishing

our previous paper, as well as the slurry and drying simulations details. The computational workflow is shown in Figure 2. Bonds are created between AM primary particles (of the same secondary particle) that are in contact in the initial microstructure.

The slurry and drying simulations are performed by using the open-source molecular dynamics simulator software LAMMPS.[54] The calendering simulations are performed in the open-source DEM software LIGGGHTS,[55] using a modified version[56] where the BPM is implemented. For simplicity, we do not consider damping for the bonds. The speed of the top plane is 0.01 m/s, close to the experimental line speed 0.009 m/s. We verified the negligible influence of this speed on the obtained pressures. A timestep of 0.01 ns (around 1.5% of Rayleigh time) was verified to give numerical stability. The simulation duration is from 2 to 9 days depending on the degree of compression. These were run in 28 cores Intel(R) Xeon(R) CPU E5-2680 v4 @ 2.40 GHz in 1 node (128 GB of RAM) of the MatriCs platform (Université de Picardie-Jules Verne, France).

Results and discussion

The parameterization of the model is performed by pressure-porosity curves resulting from experimental results as shown in Table 1. The maximum pressure during calendering is recorded in the simulation, while the porosity is calculated from the electrodes after relaxation. The calendering process is mimicked by two steps: compression and relaxation. The upper plane first moves downward with the given velocity to a certain displacement to reach the maximum compression and then moves back to the original location with the same velocity so as to achieve relaxation. Figure 3 demonstrates the 3D microstructure of one electrode before calendering and during one simulated calendering process for the same electrode until 40% of thickness reduction. The microstructures shown in the upper part are the uncalendered and calendered ones. The pressure

on the surface of the calendered microstructures are 14.2 MPa, 50.3 MPa, 98.7 MPa, and 157.7 MPa which correspond to a total thickness reduction of 10%, 20%, 30%, and 40%, respectively. The nanoporosity of CBD was set to 27%, which is similar to the porosity reported in the literature.[57] Our model introduced bonds to refer to the connection between the primary particles within the secondary particles. Although the real primary particle crystal shape is not spherical and the size is smaller than the primary particle size within the model, here, we perform a coarse-grained simulation with primary spherical particles of 1.59 μm diameter to simulate the AM mechanical behavior against the strain. At the given failure criteria, the bonds are broken to represent the disconnection between primary particles. The structures in the bottom row in Figure 3 show the state of the bonds in the secondary particles at the same compression stages as the upper row. The bond structures in the uncalendered electrode and in the calendered one at 40% of compression are compared, and the differences are indicated in light blue, which refer to the bonds broken along the compression process. The purple bonds refer to the bonds that remain intact throughout. According to the evolution of the bond structure, it can be seen that the bonds break gradually with the increase of the applied pressure. To the best of our knowledge, this is the first time that DEM simulations have been used to predict the effect of the calendering process on secondary particle fracture.

In this work, we use the experimental porosity vs. pressure profile to validate our model. As shown in Figure 4(a), the comparison of the porosity between the model results and the experimental ones at different maximum calendering pressures was obtained. The porosity of the electrode from the simulation is calculated from the volume after the relaxation process. The red and orange data points in the figure represent the porosity obtained using two different methods. The orange data points represent the porosity calculated directly from the meshing of the microstructure by using the coordinates and radius of the particles, while the red data points represent the porosity calculated from the theoretical material volume. The difference
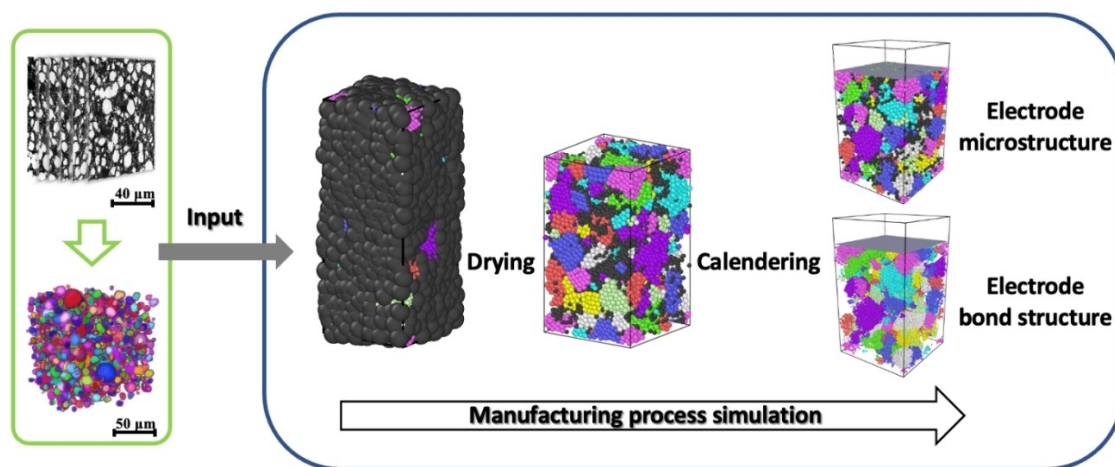

Figure 2. Computational workflow. In the simulation box, the black refers to the CBD particles and the rest colors indicate the different secondary AM particles. In the scheme for the calendering process, the bonds in the secondary particle were presented with the same color as the particle.
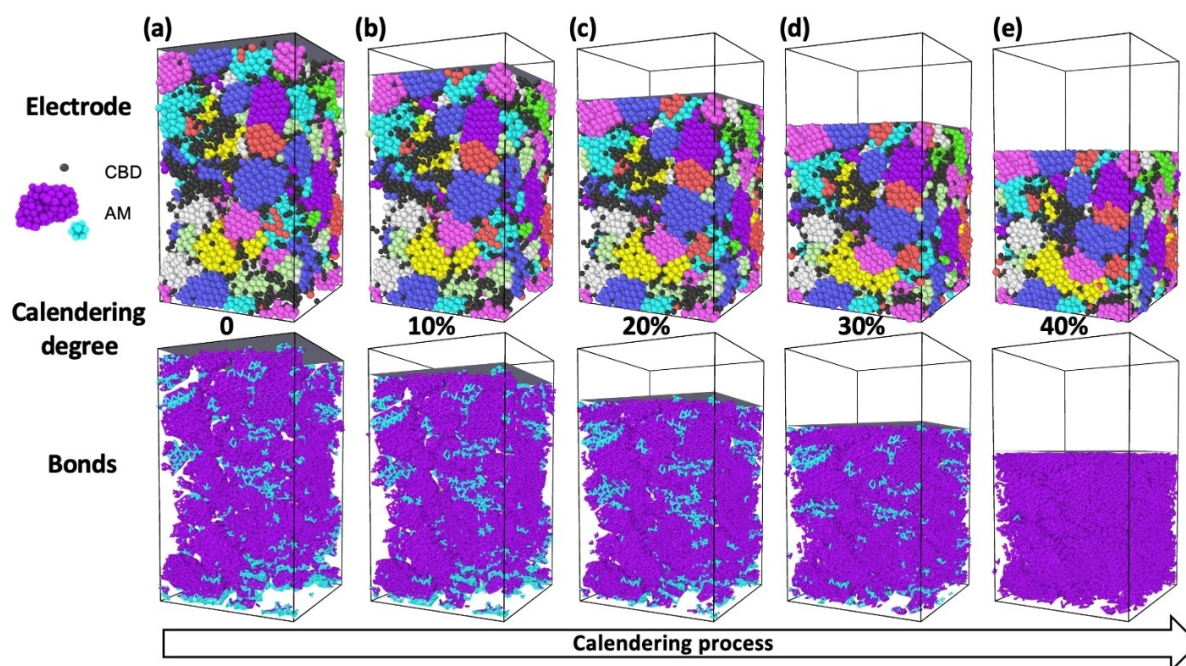
Batteries & Supercaps

Research Article
doi.org/10.1002/batt.202300371

Chemistry
Europe
European Chemical
Societies Publishing

Figure 3. The electrodes and bonds evolution during the calendering process of a maximum pressure of 150 MPa. The presented structure is the structure under the pressure of a) uncalendered, b) calendered under 9.2 MPa, c) 20.1 MPa, d) 50.9 MPa, and e) 146.8 MPa during the compression process. In the electrode structure, black indicates the CBD and the rest of the colors represent the different AM secondary particles. In the bond structure, blue indicates the bonds that will break during this compression, while purple indicates bonds that remain intact throughout.
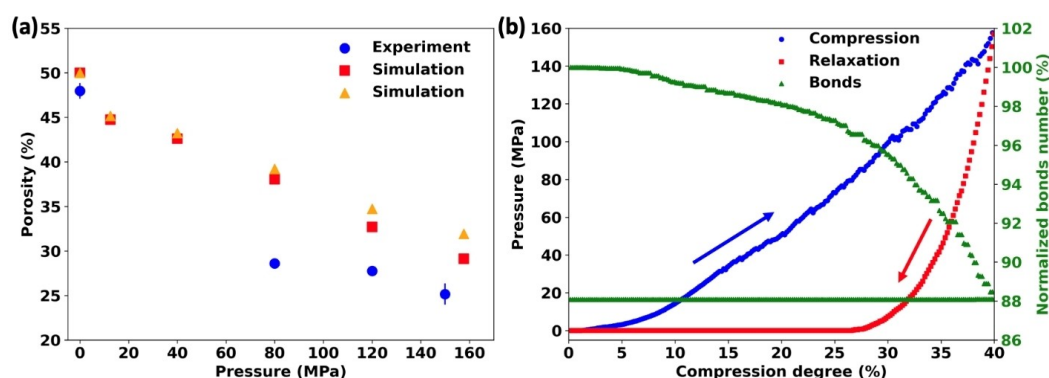
Figure 4. Mechanical and porosity validation. a) Comparison of porosity between model results and experimental values at different calendering pressures. Blue: experimental values; red: porosity calculated based on theoretical material volume; orange: porosity calculated based on microstructure meshing. b) Pressure and proportion of bond breakage vs. upper plane displacement (reduced thickness). Green: normalized number of bonds; blue: pressure applied to the electrode when it reaches the corresponding compression degree during the calendering process; red: pressure on the electrode during the relaxation process. Red points and blue points corresponding to the same 'compression degree' value indicate that the upper plane is in the same position under these conditions.

comes from the overlapping appearing after the calendering between the primary particles of AM, resulting in a higher simulation error under high calendering pressures. Overall, our simulation results have a reasonable agreement with the experimental results, demonstrating the connection between mechanical behavior and microstructure evolution of the electrodes, and solidifying our fracture prediction. Figure 4(b) demonstrates the relationship between the displacement of the upper plane and the applied pressure for the electrode calendered until 40% of compression degree. The pressure was calculated by the contact force and the contact surface area between the particles and the upper plane, the latter of which

is 910 μm². The blue curve indicates the compression process, and the red is the relaxation process. The pressure-displacement curves are consistent with the results of previously reported micro-indentation experiments.[41] It is evident that after the compression process, the electrode exhibits a spring back (relaxation process), which is a representation of the fast elastic recovery of the electrode as reported in the literature.[58] Different maximum compression degrees were simulated: the spring back degree of the electrode varies for different pressures applied to the electrode, as shown in Figure S4. In general, the higher the maximum applied pressure, the lower the spring back degree, which is similar to what has been

Batteries & Supercaps

Research Article
doi.org/10.1002/batt.202300371

Chemistry
Europe
European Chemical
Societies Publishing

reported in the literature.[27] The first point (10% of maximum compression degree) in Figure S4 does not conform to this rule, which shows a lower spring back degree. In this particular case, the pressure applied to the electrode is not high enough to reach the elastic conditions, and the microstructure evolution is mostly governed by particle rearrangement. The mechanical curves (cf. Figure 4(b)) during the compression process in the simulation are consistent with those reported in the literature.[59] For the electrode calendered until 157.7 MPa, the porosity of the entire volume was 26.72% at maximum pressure. However, after the electrode sprang back, the porosity increased to 29.12%. When comparing this value with the experimental electrode calendered under 150 MPa which has a porosity of 25.16% (cf. Figure 4(a)), the simulation results are slightly higher than the experimental results. This may be due to the inability of the simulation to capture the plastic behavior exhibited by the electrode during this process since we use an elastic contact model. The green curve (cf. Figure 4(b)) represents the proportion of broken bonds to the initial total number of bonds during this process. The result shows that approximately 1.8%, 4.5%, and 11.1% of the bonds are broken when the pressure reaches 50 MPa, 100 MPa, and 150 MPa, respectively. Almost all bond fractures occur under the stress of compression during the calendering process, while only a negligible number of bonds undergo changes during electrode relaxation. The latter accounts for 3% of the total bond fractures, which may be attributed to the interaction forces among the AM secondary particles during the rearrangement in the relaxation process.

From our experimental observations, not all secondary particles have fractures under this pressure. Through our model, it can be seen that for 10% compression degree, most of the cracks appear in bigger particles, as shown in Figure S5. It has an agreement with the experimental report that bigger secondary particles will break first.[15] Here we have selected one of the most likely fractured secondary particles to study the evolution of its shape and internal structure. Since the nano-fracture we observe is smaller than the scale of our model, we are not able to observe the fracture of the secondary particle from the simulation results. Figure 5 shows the evolution of an AM particle from the lower-middle region of the electrode with an equivalent diameter of 11.96 μm during the 40% compression process. Similarly, the bonds inside this secondary particle in the uncalendered electrode and in the electrode of 40% compression are compared, and the differences are indicated in light blue. The location of it is indicated in Figure 5a. For this large secondary particle consisting of 426 primary particles, it initially has 1748 bonds in the simulation. After the calendering, it can be seen that there is a slight deformation of the particle due to the force, which is accompanied by the bond breakage. The blue curve in Figure 5b provides the pressure experienced by the electrode along the calendering simulation. The purple points correspond to the particles shown in Figure 5c and Figure 5d, and their corresponding calendering pressures are given at the bottom. The green curve shows the normalized bond number contained in the AM secondary particle and its change during the simulation. The particle exhibits noticeable bond breakage only when the electrode is subjected to a calendering pressure of the electrode exceeding 120 MPa and
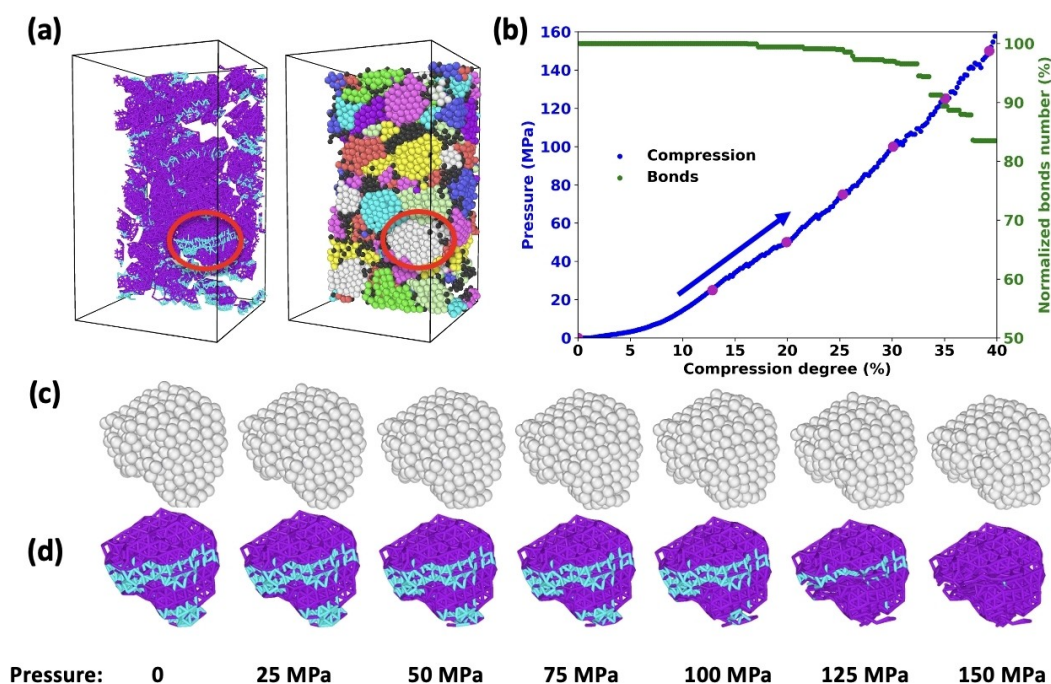

Figure 5. Study of a selected individual particle with a high ratio of bond breaks and its possible cracks. a) Cross-sectional diagram of the volume. The position of the studied particles within the electrode is indicated. b) The pressure applied on the simulated electrode and the number of bonds break of this individual particle. c) Particle shape evolution during the calendering. d) The change of the bonds within the selected particle during the calendering. The blue indicates the bonds that will break during this compression, while purple indicates bonds that remain intact throughout.

has 17% bonds break after 40% compression degree. Combined with our Nano-XCT images observed at 150 MPa (Figure 1b) and the individual particle study (Figure 5d), we can speculate that in the model, secondary particle cracking occurs when the number of broken bonds is approximately above 10%, i.e., when the applied pressure is approximately above 120 MPa. The location of the bond breakage is not uniformly distributed in the electrode. This location is related to the distribution or orientation of the particles in the electrode and the force applied. Also, the number of bond breaks is not linearly related to the reduction of the thickness due to the uneven force inside the electrode, as shown in Figure 4(b). Similarly, particles located near the current collector (Figure S6) and near the top surface (Figure S7) of the electrode were also selected for study. It was observed that particles near the current collector experienced earlier bond breakage at below 10 MPa and exhibited noticeable deformation when the electrode was subjected to a pressure of 75 MPa. This could be attributed to its proximity to the current collector, which limited its ability to undergo corresponding displacement and rotation in the electrode's self-organization process in response to pressure. On the other hand, particles closer to the electrode surface exhibited higher flexibility within the microstructure, resulting in fewer bond breakages, even under high pressure, with less than 10% of bonds being fractured. A study of bond breakage of AM particles in various parts of the electrode is shown in Figure S8. The electrodes in the simulation are divided into 3 parts from the surface to the current collector side: top, middle, and bottom. It can be seen that the zone with the highest number of bond breaks is located in the bottom region. In addition, bond breakage occurs just after calendering starts, which indicates that cracks can appear in the particles even at the beginning of calendering or low-pressure calendering. This is consistent with the fact that even for the first stages of calendering cracks can appear.[15] It is also reported that the cracks are more likely to appear in regions where the curvature is higher,[60] which is also corroborated in our model by the particles shown in Figure 5 and Figure S8. These observations are qualitative, in future work, a fully calibrated model will allow to elucidate the crack propagation trajectories in the electrode during calendering. Furthermore, due to the scale limitation, we cannot observe the fracture and the reintegration of the material due to the binder after the fracture generation, which, according to the literature,[13] is a possible occurrence and contributes to the electrode's resistance to the capacity decay after electrochemical cycling.

Conclusions

In this work, we have first precisely assessed the fracture of NMC111 secondary particles due to pressure during the calendering process of the LIB electrodes through *ex situ* nano-XCT experiments, and the cracks are 3D visualized. From this, we developed a 3D LIB electrode calendering model using DEM based on the real AM particle shape obtained by micro XCT. The model allows to predict the mechanical behavior of the

particles under pressure during compression. The initial uncalendered electrode microstructure was derived from the results of our previous work using a CGMD-based physical model for simulating slurry and drying. In this new work, bonds between primary particles are introduced into the electrode microstructure for each secondary particle, in order to simulate the connection of the primary particles. This work reports the calendering and the relaxation of a single formulation under different pressure conditions in the range of 0-157 MPa, and the obtained electrode porosity values for the simulation are in reasonable agreement with the experimental results. It is found that the breakage of the bonds does not depend linearly on the applied force. With the increase of the pressure and the decrease of the electrode porosity, the source of the microstructural change in the electrode changes from the movement of particles to the deformation and fracture of particles. This novel method enables us to focus on the generation of internal fractures within individual secondary particles. Through XCT experiments and computational simulations, it is able to calibrate the criteria of bond breakage numbers leading to secondary particle fracture. Thus, the model becomes capable of forecasting the generation of fractures in secondary particles. In the future, the microstructures obtained from the model will be used in a finite element method simulator to capture the subtle effects of particle deformation and fracture on the electrochemical performance. Our model can also be applied to other materials and chemistries, which we believe will be instructive for the entire battery community and industry in particular.

Supporting Information

A file containing the supplementary information and details of the experiments and the model, and supplementary results figures (PDF).

A video showing particle details (MP4).

A video showing structure change during the calendering simulation (MP4).

A video showing bonds change during the calendering simulation (MP4).

Batteries & Supercaps

Research Article
doi.org/10.1002/batt.202300371

Chemistry
Europe

European Chemical
Societies Publishing

Conflict of Interests

The authors declare no conflict of interest.

Data Availability Statement

The data that support the findings of this study are available from the corresponding author upon reasonable request.

[1] G. Zubi, R. Dufo-López, M. Carvalho, G. Pasaoglu, *Renewable Sustainable Energy Rev.* **2018**, *89*, 292.
[2] S. N. Bryntesen, A. H. Strømman, I. Tolstorebrov, P. R. Shearing, J. J. Lamb, O. Stokke Burheim, *Energies* **2021**, *14*, 1406.
[3] A. Kwade, W. Haselrieder, R. Leithoff, A. Modlinger, F. Dietrich, K. Droeder, *Nat. Energy* **2018**, *3*, 290.
[4] H. Zheng, L. Tan, G. Liu, X. Song, V. S. Battaglia, *J. Power Sources* **2012**, *208*, 52.
[5] A. Davoodabadi, J. Li, H. Zhou, D. L. Wood, T. J. Singler, C. Jin, *J. Energy Storage* **2019**, *26*, 101034.
[6] Y. Sheng, C. R. Fell, Y. K. Son, B. M. Metz, J. Jiang, B. C. Church, *Front. Energy Res.* **2014**, *2*, DOI 10.3389/fenrg.2014.00056.
[7] E. N. Primo, M. Chouchane, M. Touzin, P. Vazquez, A. A. Franco, *J. Power Sources* **2021**, *488*, 229361.
[8] E. N. Primo, M. Touzin, A. A. Franco, *Batter. Supercaps* **2021**, *4(5)*, 834–844, batt.202000324.
[9] G. Lenze, F. Röder, H. Bockholt, W. Haselrieder, A. Kwade, U. Krewer, *J. Electrochem. Soc.* **2017**, *164*, A1223.
[10] C. Liu, T. Lombardo, J. Xu, A. C. Ngandjong, A. A. Franco, *Energy Storage Materials* **2023**, *54*, 156–163.
[11] X. Lu, S. R. Daemi, A. Bertei, M. D. R. Kok, K. B. O'Regan, L. Rasha, J. Park, G. Hinds, E. Kendrick, D. J. L. Brett, P. R. Shearing, *Joule* **2020**, *4*, 2746.
[12] M. Ebner, D.-W. Chung, R. E. García, V. Wood, *Adv. Energy Mater.* **2014**, *4*, 1301278.
[13] R. Sim, S. Lee, W. Li, A. Manthiram, *ACS Appl. Mater. Interfaces* **2021**, *13*, 42898.
[14] L. Bläubaum, F. Röder, C. Nowak, H. S. Chan, A. Kwade, U. Krewer, *ChemElectroChem* **2020**, *7*, 4755.
[15] F. Huttner, A. Diener, T. Heckmann, J. C. Eser, T. Abali, J. K. Mayer, P. Scharfer, W. Schabel, A. Kwade, *J. Electrochem. Soc.* **2021**, *168*, 090539.
[16] M. Ebner, F. Geldmacher, F. Marone, M. Stampanoni, V. Wood, *Adv. Energy Mater.* **2013**, *3*, 845.
[17] X. Lu, A. Bertei, D. P. Finegan, C. Tan, S. R. Daemi, J. S. Weaving, K. B. O'Regan, T. M. M. Heenan, G. Hinds, E. Kendrick, D. J. L. Brett, P. R. Shearing, *Nat. Commun.* **2020**, *11*, 2079.
[18] T. Nguyen, J. Villanova, Z. Su, R. Tucoulou, B. Fleutot, B. Delobel, C. Delacourt, A. Demortière, *Adv. Energy Mater.* **2021**, *11*, 2003529.
[19] J. B. Robinson, J. A. Darr, D. S. Eastwood, G. Hinds, P. D. Lee, P. R. Shearing, O. O. Taiwo, D. J. L. Brett, *J. Power Sources* **2014**, *252*, 51.
[20] Z. Liu, J. Scott Cronin, Y. K. Chen-Wiegart, J. R. Wilson, K. J. Yakal-Kremski, J. Wang, K. T. Faber, S. A. Barnett, *J. Power Sources* **2013**, *227*, 267.
[21] A. G. Kashkooli, S. Farhad, D. U. Lee, K. Feng, S. Litster, S. K. Babu, L. Zhu, Z. Chen, *J. Power Sources* **2016**, *307*, 496.
[22] Z. Su, E. Decencière, T.-T. Nguyen, K. El-Amiry, V. De Andrade, A. A. Franco, A. Demortière, *Npj Comput. Mater.* **2022**, *8*, 30.
[23] S. R. Daemi, C. Tan, T. G. Tranter, T. M. M. Heenan, A. Wade, L. Salinas-Farran, A. V. Llewellyn, X. Lu, A. Matruglio, D. J. L. Brett, R. Jervis, P. R. Shearing, *Small Methods* **2022**, *6*, 2200887.
[24] A. A. Franco, A. Rucci, D. Brandell, C. Frayret, M. Gaberscek, P. Jankowski, P. Johansson, *Chem. Rev.* **2019**, *119*, 4569.
[25] E. Ayerbe, M. Berecibar, S. Clark, A. A. Franco, J. Ruhland, *Adv. Energy Mater.* **2021**, 2102696.
[26] F. M. Zanotto, D. Z. Dominguez, E. Ayerbe, I. Boyano, C. Burmeister, M. Duquesnoy, M. Eisentraeger, J. F. Montaño, A. Gallo-Bueno, L. Gold, F. Hall, N. Kaden, B. Muerkens, L. Otaegui, Y. Reynier, S. Stier, M. Thomitzek, A. Turetskyy, N. Vallin, J. Wessel, X. Xu, J. Abbasov, A. A. Franco, *Batteries & Supercaps* **2022**, *5*, e202200224.
[27] C. Sangrós Giménez, B. Finke, C. Schilde, L. Froböse, A. Kwade, *Powder Technol.* **2019**, *349*, 1.
[28] I. Srivastava, D. S. Bolintineanu, J. B. Lechman, S. A. Roberts, *ACS Appl. Mater. Interfaces* **2020**, *12*, 34919.
[29] M. Nikpour, N. Barrett, Z. Hillman, A. I. Thompson, B. A. Mazzeo, D. R. Wheeler, *J. Electrochem. Soc.* **2021**, *168*, 060547.
[30] M. Nikpour, B. A. Mazzeo, D. R. Wheeler, *J. Electrochem. Soc.* **2021**, *168*, 120518.
[31] R. Ge, D. J. Cumming, R. M. Smith, *Powder Technol.* **2022**, *403*, 117366.
[32] R. Ge, A. M. Boyce, Y. Shui Zhang, P. R. Shearing, D. J. Cumming, R. M. Smith, *Chem. Eng. J.* **2023**, *465*, 142749.
[33] M. Lippke, J. Meister, C. Schilde, A. Kwade, *Processes* **2022**, *10*, 1667.
[34] Z. Wang, L. Yang, S. Zhu, W.-L. Song, H.-S. Chen, *Extreme Mech. Lett.* **2021**, *46*, 101252.
[35] E. Asylbekov, R. Trunk, M. J. Krause, H. Nirschl, *Energy Technol.* **2021**, *9*, 2000850.
[36] A. Lundkvist, P.-L. Larsson, E. Olsson, *Powder Technol.* **2023**, *425*, 118574.
[37] "ERC Artistic: Home," can be found under http://www.erc-artistic.eu/.
[38] A. C. Ngandjong, A. Rucci, M. Maiza, G. Shukla, J. Vazquez-Arenas, A. A. Franco, *J. Phys. Chem. Lett.* **2017**, *8*, 5966.
[39] T. Lombardo, J. Hoock, E. N. Primo, A. C. Ngandjong, M. Duquesnoy, A. A. Franco, *Batteries & Supercaps* **2020**, *3*, 721.
[40] T. Lombardo, A. C. Ngandjong, A. Belhcen, A. A. Franco, *Energy Storage Mater.* **2021**, *43*, 337.
[41] A. C. Ngandjong, T. Lombardo, E. N. Primo, M. Chouchane, A. Shodiev, O. Arcelus, A. A. Franco, *J. Power Sources* **2021**, *485*, 229320.
[42] M. Chouchane, A. Rucci, T. Lombardo, A. C. Ngandjong, A. A. Franco, *J. Power Sources* **2019**, *444*, 227285.
[43] T. Lombardo, F. Caro, A. C. Ngandjong, J.-B. Hoock, M. Duquesnoy, J. C. Delepine, A. Ponchelet, S. Doison, A. A. Franco, *Batteries & Supercaps* **2022**, *5*, e202100324.
[44] J. Xu, A. C. Ngandjong, C. Liu, F. M. Zanotto, O. Arcelus, A. Demortière, A. A. Franco, *J. Power Sources* **2023**, *554*, 232294.
[45] T. Weitkamp, M. Scheel, J. Perrin, G. Daniel, A. King, V. L. Roux, J. L. Giorgetta, A. Carcy, F. Langlois, K. Desjardins, C. Menneglier, M. Cerato, C. Engblom, G. Cauchon, T. Moreno, C. Rivard, Y. Gohon, F. Polack, *J. Phys. Conf. Ser.* **2022**, *2380*, 012122.
[46] M. Scheel, J. Perrin, F. Koch, G. Daniel, J. L. Giorgetta, G. Cauchon, A. King, V. Yurgens, V. L. Roux, C. David, T. Weitkamp, *J. Phys. Conf. Ser.* **2022**, *2380*, 012045.
[47] A. Mirone, E. Brun, E. Gouillart, P. Tafforeau, J. Kieffer, *Nucl. Instrum. Methods Phys. Res. Sect. B Beam Interact. Mater. At.* **2014**, *324*, 41.
[48] I. Arganda-Carreras, V. Kaynig, C. Rueden, K. W. Eliceiri, J. Schindelin, A. Cardona, H. Sebastian Seung, *Bioinformatics* **2017**, *33*, 2424.
[49] "Avizo Software | Materials Characterization Software - FR," can be found under http://www.thermofisher.com/fr/fr/home/electron-microscopy/software/software-em-3d-vis/avizo-software.html.
[50] P. A. Cundall, O. D. L. Strack, *Géotechnique* **1979**, *29*, 47.
[51] D. O. Potyondy, P. A. Cundall, *Int. J. Rock Mech. Min. Sci.* **2004**, *41*, 1329.
[52] Y. Guo, J. Curtis, C. Wassgren, W. Ketterhagen, B. Hancock, *AIP Conf. Proc.* **2013**, *1542*, 491.
[53] D. André, M. Jebahi, I. Iordanoff, J. Charles, J. Néauport, *Comput. Methods Appl. Mech. Eng.* **2013**, *265*, 136.
[54] A. P. Thompson, H. M. Aktulga, R. Berger, D. S. Bolintineanu, W. M. Brown, P. S. Crozier, P. J. in 't Veld, A. Kohlmeyer, S. G. Moore, T. D. Nguyen, R. Shan, M. J. Stevens, J. Tranchida, C. Trott, S. J. Plimpton, *Comput. Phys. Commun.* **2022**, *271*, 108171.
[55] C. Kloss, C. Goniva, A. Hager, S. Amberger, S. Pirker, *Prog. Comput. Fluid Dyn. Int. J.* **2012**, *12*, 140.

[56] M. Schramm, M. Z. Tekeste, C. Plouffe, D. Harby, *Biosyst. Eng.* **2019**, *186*, 349.

[57] S. R. Daemi, C. Tan, T. Volkenandt, S. J. Cooper, A. Palacios-Padros, J. Cookson, D. J. L. Brett, P. R. Shearing, *ACS Appl. Energ. Mater.* **2018**, *1*, 3702.

[58] A. Diener, S. Ivanov, W. Haselrieder, A. Kwade, *Energy Technol.* **2022**, *10*, 2101033.

[59] J. Zhang, J. Sun, H. Huang, Z. Yuan, *Particuology* **2023**, *85*, 252–267.

[60] Y. K. Chen-Wiegart, Z. Liu, K. T. Faber, S. A. Barnett, J. Wang, *Electrochem. Commun.* **2013**, *28*, 127.